2D-MoS2

Two-dimensional (2D) materials are generally defined as crystalline substances with a few atoms thickness.Two-dimensional transition metal dichalcogenide (2D-TMDs) semiconducting (SC) materials have exhibited unique optical and electrical properties. The layered configuration of the 2D-TMDs materials is at the origin of their strong interaction with light and the relatively high mobility of their charge carriers, which in turn prompted their use in many optoelectronic applications, such as ultra-thin field-effect transistors, photo-detectors, light emitting diode, and solar-cells. Generally, 2D-TMDs form a family of graphite-like layered thin semiconducting structures with the chemical formula of MX2, where M refers to a transition metal atom (Mo, W, etc.) and X is a chalcogen atom (Se, S, etc.). The layered nature of this class of 2D materials induces a strong anisotropy in their electrical, chemical, mechanical, and thermal properties. In particular, molybdenum disulfide (MoS2) is the most studied layered 2D-TMD.

1. MoS$_2$

From a crystalline point of view, layered MoS$_2$ exists in three polymorphic crystalline structures: 1T (tetragonal) [1], 2H (hexagonal) [2], and 3R (rhombohedral) [3] (Figure 1). The crystallographic parameters associated to these crystalline forms are summarized in Table 1. In the case of mono- to few-layer structures, 2H-MoS$_2$ is the most thermodynamically stable phase and thus the most commonly encountered. When the MoS$_2$ is in the monolayer form, it takes an octahedral or a trigonal prismatic coordination phase.
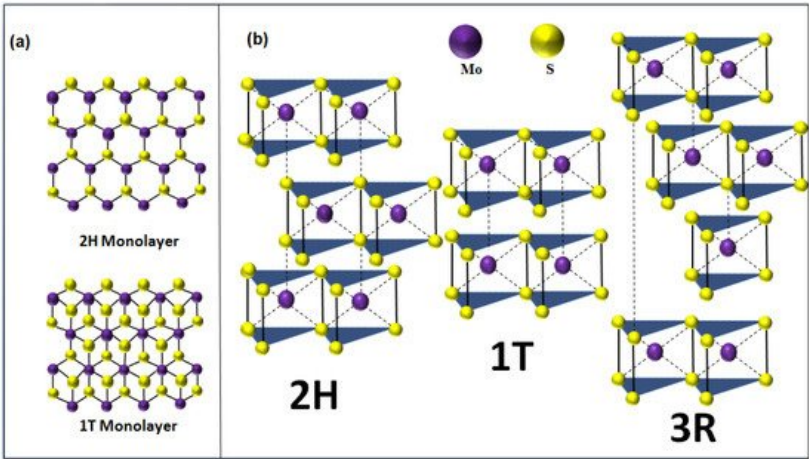

Figure 1. (**a**) Top view of 2H/1T MoS$_2$ monolayer. (**b**) Polymorphic structures of MoS$_2$ (2H is the hexagonal crystal form, 1T is the tetragonal crystal form, and 3R is the rhombohedral crystal form).

Table 1. Crystal parameters and the nature of polymorphic structures of 2D-MoS$_2$.

Polymorphic Structure	Lattice Parameter	Point Group	Electronic Behavior	Ref
1T	a = 5.60 Å, c = 5.99 Å	D$_{6d}$	Metal	[1]
2H	a = 3.15 Å, c = 12.30 Å	D$_{6h}$	Semiconductor	[2]
3R	a = 3.17 Å, c = 18.38 Å.	C$_{3v}$	Semiconductor	[3]

Furthermore, MoS$_2$ layered materials were observed to exhibit various shapes and morphologies, such as planar [4][5][6] and vertically aligned nanosheets (NSs) [7], nanoflowers [8], nanotubes [9], nanowires [10], and nanoplatelets [11][12]. This variety of forms could be controlled by choosing suitable synthesis routes with optimized operating parameters [8][9][10][11] [13][14][15][16][17]. Thus, it is possible to adjust the 2D-MoS$_2$ properties to develop high performance devices i energy storage [17], electronics [16], photonics [15], sensing [18], and field emission [19] applications. Recently, up to few-layer MoS$_2$ nanosheets have been shown to be highly efficient for electronic, optoelectronic, and solar energy harvesting devices [20][21][22] because of their tunable direct bandgap [23], strong light-absorption, and prominent photoluminescence with energies lying in the visible range (1.8–1.9 eV) [24].

Although Mo and S are strongly covalently bonded within an individual layer, adjacent sheets are linked together only by the very weak van der Waals interaction. This weak bonding provides a facile processing route such as mechanical or chemical exfoliation to form few- to monolayer MoS$_2$ films. Unlike graphene, 2D-MoS$_2$ is much less prone to surface contaminations, which offers a superior chemical stability to 2D-MoS2, making it more attractive for the above-mentioned applications [25][26][27].

2. Fabrication Techniques of 2D-MoS$_2$

Tremendous efforts have been devoted to the synthesis of 2D-MoS$_2$ with controllable large-area growth and uniform atomic layers using both top-down and bottom-up approaches. The most commonly used processing routes are detailed in the following sub-sections along with their advantages and limitations.

2.1. Mechanical and Chemical Exfoliations

Mechanical exfoliation, also known as micromechanical cleavage, is a straightforward technique that takes advantage of the weak bonding between layers, for the production of high-quality mono- to few-layer MoS$_2$ [28][29][30]. It consists of exfoliating thin films of 2D-MoS$_2$ from a bulk MoS$_2$ crystal by using a low surface tension tape to break the weak interlayer bonds in a similar way as for grapheme [31]. Additional exfoliation of the extracted films may be needed to obtain few- to monolayer MoS$_2$. Tapes could be attached to glass slides to achieve planar exfoliation and slow peeling. The obtained monolayers are usually transferred to an appropriate substrate for further analysis and testing.

The advantage of the mechanical exfoliation process lies in its simplicity that requires the sole use of a confocal microscope to localize the 2D-MoS$_2$ layers deposited on the substrate. Conveniently, this technique can produce high crystalline quality mono- to few layers with a lateral size up to few tens of micrometers, making them highly suitable for sensing applications. However, this approach suffers from a lack of a consistent control in producing the 2D monolayers as it is heavily user-dependent and does not permit the control of the size and/or thickness uniformity of the exfoliated 2D-MoS$_2$ layers [32]. Therefore, the mechanical exfoliation technique is not necessarily suitable for the production of 2D-MoS$_2$ layers intended for large-area and high-throughput applications.

Chemical exfoliation, on the other hand, appears as a promising approach to produce large quantities of mono- and few-layer MoS$_2$ nanosheets [30][33][34][35]. Eda et al. [24] reported a high yield of monolayer crystal synthesis using chemical exfoliation of bulk MoS$_2$ via Li intercalation. However, this approach may induce an alteration in the quality of the produced 2D-MoS$_2$. For instance, the chemically exfoliated MoS$_2$ layers can lose their semiconducting properties because of the structural changes resulting from the Li intercalation process. However, this fabrication route stands by its ease of processing, low production costs, and suitability for catalysis and/or sensing applications [36].

2.2. Chemical Vapor Deposition

Chemical vapor deposition (CVD) is one of the most popular routes for large-scale, high-quality, and low-cost 2D-MoS$_2$ material production [19][37][38][39]. CVD is a bottom-up fabrication method at the equilibrium state, which enables the processing of layered 2D-MoS$_2$ with controlled morphology and good crystallinity while minimizing structural defects. The control of the CVD process is ensured by tuning the deposition parameters such as temperature, pressure, gas flow rate, precursor's quantities, and substrate types. The 2D-MoS$_2$ synthesis via the CVD technique can be achieved by means of thermal vapor sulfurization (TVS), thermal vapor deposition (TVD), and thermal decomposition (TD). Deokar et al. [13] used TVS for high quality and vertically-aligned luminescent MoS$_2$ nanosheets. A similar process could be used to grow 2D-MoS$_2$ layers [6][40] by employing two sources, such as molybdenum thin film (below 20 nm) or molybdenum oxide (MoO$_3$) powder deposited on a SiO$_2$/Si substrate as a first precursor and the sulfur powder or gaseous sulfur source (H$_2$S, etc.) as the second precursor [19][37][38][39][41][42]. A typical CVD sulfurization process (Figure 2a) is usually performed in a tubular furnace reactor, where a continuous argon flow (typical flow rate 100 sccm) is used as a carrier gas to stream the evaporated sulfur into the Mo source materials.
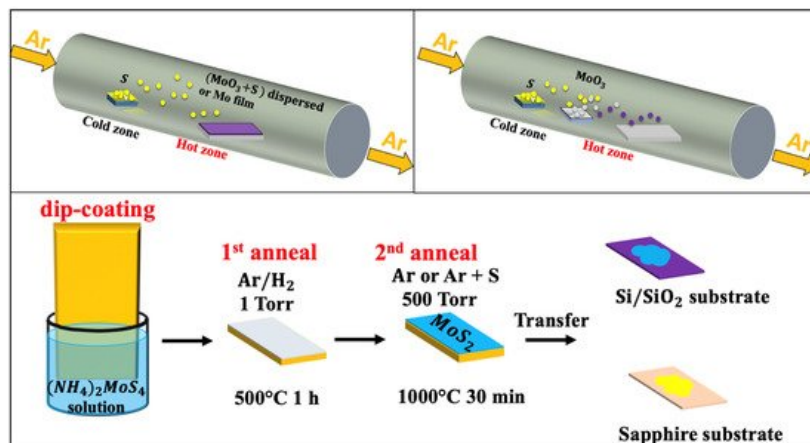
Figure 2. Schematic of the chemical vapor deposition techniques: (**a**) thermal vapor sulfurization process using a quartz tube; (**b**) thermal vapor deposition process using a quartz tube; and (**c**) thermal decomposition of $(NH_4)_2MoS_4$ (reproduced and adapted from Ref. [4]).

One of the critical aspects to be controlled in such a CVD tubular reactor is the temperature gradient between the S powder and the substrate. In fact, while the S powder is at 150–200 °C, the substrate's temperature—with or without Mo thin film—should be maintained in the 700–900 °C range to obtain the 2D-MoS_2 phase. This technique offers sufficient latitude to fairly control the thickness and the homogeneity of the grown 2D-MoS_2. The typical average lateral crystal size obtained by CVD is usually in the 10–30 nm range. Table 2 shows few examples of CVD-TVS grown MoS_2 nanostructures along with their associated processing conditions.

Table 2. Examples of CVD-TVS grown MoS_2 nanostructures.

Substrate	Precursors	Growth Conditions	Morphology	Ref
Si	MoO_3 and S powders dispersed on substrate	MoO_3 and S powders dispersed on substrate at 850 °C; S powder at 400 °C; Ar-0.725 L/min; time reaction = 30 min	MoS_2 nanosheets	[13]
Si [001]	S powder and Mo film deposited on substrate	Mo deposited on Silicon at 850 °C, S at 400 °C; Ar-0.725 L/min; time reaction = 30 min	MoS_2 nanosheets	[14]
Si/SiO$_2$	S powder and Mo film deposited on substrate	Mo deposited on Silicon at 850 °C, S at 400 °C; Ar-0.725 L/min; time reaction = 30 min	MoS_2 nanosheets	[19]
Diamond substrate	S powder and Mo deposited on substrate	Mo deposited on Silicon with S powder at 800 °C; N_2; ambient pressure; time reaction = 30 min	Horizontally and vertically MoS_2	[43]
Si/SiO$_2$	S powder and MoO_3 deposited on substrate	MoO_3 film deposited on Silicon at 750–850 °C, 600 mg of S powder at 100 °C; Ar-0.01 L/min; time reaction = 10 min	Mono-to few-layers of MoS_2	[44]

Table 2 shows the typical morphologies obtained for MoS_2, which seem to depend on the carrier gas and the type of the substrate used. The reaction time and the spatial position of the substrate strongly affect the number of resulting layers.

The TVD based MoS_2 growth (Figure 2b) involves the concomitant evaporation of both MoO_3 and S powders. This approach consists of a stepwise sulfurization of MoO_3 to form the MoS_2 phase. It has been shown that, by increasing the S vapor flux, the sulfurization proceeds through several phase changes before reaching the final product. First, MoO_3 is formed, then MoO_2 followed by $MoOS_2$, and finally MoS_2. This approach is very useful to obtain 2D MoS_2 layers with a lateral size of few tens of microns. The TVD growth conditions of MoS_2 under various conditions and with different characteristics are summarized in Table 3.

Table 3. Examples of TVD grown MoS_2 along with their relevant processing conditions (* D is the distance between the MoO_3 and s powders inside the tubular furnace).

Substrate/Setup	MoO$_3$ (mg)	S (mg)	D * (cm)	Gas, Flow (sccm)	T (°C), Time (min)	Morphology	Ref
Si face-down	15	80	18	Ar 10 to 500	700, 30	Flake size between 5.1–47.9 µm	[45]
SiO$_2$/Si face-up	10	200	30	Ar, 100	850, 20	Monolayer, bilayer and trilayer MoS_2	[46]

Substrate/Setup	MoO$_3$ (mg)	S (mg)	D * (cm)	Gas, Flow (sccm)	T (°C), Time (min)	Morphology	Ref
SiO$_2$/Si face-down	10	100	–	N$_2$, 20	650, 20	MoS$_2$ monolayer	[47]
SiO$_2$/Si face-down	10-30	–	25	Ar, 150	800, 10	MoS$_2$ triangular flakes	[48]
SiO$_2$/Si face-up	50	175	–	N$_2$, 300	750, 15	MoS$_2$ monolayer with lateral size of 50 µm	[49]

In comparison to the results obtained by CVD-TVS summarized in Table 2, TVD exhibits high-yield fabrication of 2D-MoS$_2$ monolayers generally exhibiting a triangular flakes shape. Besides, one can notice the two possible configurations of the substrate of interest in TVD face-up and face-down compared to CVD-TVS [45][46][47][48][49].

Moreover, the TD-based CVD method presents an alternative approach to produce highly crystalline MoS$_2$ thin layers with superior electrical properties on insulating substrates [4]. Typically, the TD-CVD is based on the high-temperature annealing of a thermally decomposed ammonium thiomolybdate layer (NH$_4$)$_2$MoS$_4$ in the presence of S, as illustrated in Figure 2c. It is worth noting that the excess in sulfur introduces changes in the shape, size, and morphology of fabricated MoS$_2$. It also leads to a p-type MoS$_2$ semiconductor by increasing the electrons deficiency. In contrast, the presence of sulfur vacancies in MoS$_2$ was reported to have a direct impact on the catalytic properties of MoS$_2$, suggesting a carriers' mobility alteration [50]

Besides, the addition of S during the high-temperature annealing drastically enhances the crystallinity of MoS$_2$. Relatively, centimeter-sized MoS$_2$ crystals could be formed on Al$_2$O$_3$ substrates compared to SiO$_2$ ones [5]. The fully covered Al$_2$O$_3$ substrate with an epitaxial monolayer of MoS$_2$ was achieved at 930 °C. The MoS$_2$ crystals nucleate in a single domain to pursue by domain-to-domain stitching process occurring during annealing at 1000 °C mediated by the oxygen flow. The difference in the self-limited monolayer growth observed between the SiO$_2$ and Al$_2$O$_3$ substrates is related to the absorption energy barrier on MoS$_2$ [7]. In particular, the growth of MoS$_2$ on Al$_2$O$_3$ obeys the surface-limited epitaxial growth mode, which is not the case for the SiO$_2$ due to lattice mismatch. Moreover, the patterning of the as-grown MoS$_2$ layers has been reported by means of the polydimethylsiloxane (PDMS) stamps and the reuse of the substrate after transferring the MoS$_2$ layers [5]. Recently, the epitaxial growth of centimeter wafer-scale single-crystal MoS$_2$ monolayers on vicinal Au (111) thin films were also obtained at a processing temperature of 720 °C, by melting and re-solidifying commercial Au foils [6]. This allows overcoming the evolution of antiparallel domains and twin boundaries, leading to the formation of polycrystalline films. It has been proposed that the step edge of Au (111) induced the unidirectional nucleation, growth, and subsequent merging of MoS$_2$ monolayer domains into single-crystalline films.

2.3. Atomic Layer Deposition

The atomic layer deposition (ALD) technique is known to produce high-quality thin films even at low temperatures, typically between 150 and 350 °C. Since ALD is an atom stepwise growth process, where the reactants are alternately injected into the growth area, it allows the purging of excess species and by-products after each reaction. As a result, high-quality films are obtained by sequential surface reactions. A schematic representation of the ALD synthesis of 2D-MoS$_2$ can be found elsewhere [51].

Despite the challenges related to its synthesis conditions, ALD makes it possible to deposit crystalline MoS$_2$ thin films at a relatively low temperature (<350 °C) followed by annealing. For instance, L.K. Tan et al. [52] reported the possibility to use ALD for the synthesis of highly crystallized MoS$_2$ films on sapphire substrates at 300 °C. They prepared MoS$_2$ films by alternating exposure of the substrate to Mo(V) chlorides (MoCl$_5$) and hydrogen disulfide (H$_2$S) vapors. Similarly, Mattinen et al. [53] proposed the use of a Mo based precursor, namely Mo(thd)$_3$ (thd = 2,2,6,6 tetramethylheptane 3,5-dionato), with H$_2$S as a sulfur source. They have been able to achieve a self-limiting growth and a linear film thickness control (with a very low growth rate of ≈0.025 Å per cycle). While the crystallinity of these MoS$_2$ films was found to be particularly good (taking into account that the deposition was done at a low temperature), their surface was rather rough, consisting of flake-like grains with a size of ≈10–30 nm. One of the advantages of this process is the possibility to deposit layered MoS$_2$ films on various substrates. Table 4 summarizes the main processing conditions used by different groups along with the achieved MoS$_2$ film thicknesses.

Table 4. Summary of the ALD deposition conditions and achieved MoS$_2$ film thicknesses.

Substrate	Precursors	P (Torr)	T (°C)	Cycles	Thickness	Ref
SiO_2/Si	Mo hexacarbonyl and dimethyldisulfide	1.4–3.3	100	100	≈11 nm	[54]
SiO_2/n-Si	$MoCl_5$ and H_2S	0.75	350–450	100	≈9 nm	[55]
Al_2O_3	$Mo(NMe_2)_4$ and H_2S	–	60	100	≈12 nm	[51]
Al_2O_3 2-inch wafer	$MoCl_5$ and H_2S	0.001	300	50	≈9 nm	[52]
SiO_2/Si	$Mo(thd)_3$ (thd = 2,2,6,6 tetramethylheptane 3,5-dionato) and H_2S	3.75	300	100	≈25 nm	[53]
Al_2O_3 c-plane	$MoCl_5$ and hexamethyldisilathiane	3.75	350	250	≈22 nm	[56]
Carbon nanotubes, Si-wafers and glass	bis(tbutylimino)bis(dimethylamino) Mo (VI) and H_2S	300	100–250	100	≈11 nm	[57]
Si, SiO_2, Al_2O_3	$MoCl_5$ and H_2S	3.75	430–480	1	1 layer	[58]
Si	$MoCl_5$ and H_2S	–	390–480	100	≈21.5 nm	[59]
SiO_2	Mo hexacarbonyl and H_2S	–	175	100	≈5 nm	[60]

The ALD appears as a potentially interesting technique for the production of high-quality MoS_2 ultrathin films at relatively low temperatures and with the ability to achieve excellent step coverage onto different substrates. However, the very low throughput of the ALD might hinder its scalability and competitiveness in comparison with other physical and/or chemical deposition methods.

2.4. Pulsed Laser Deposition

Pulsed laser deposition (PLD) has emerged as one of the most promising physical vapor deposition (PVD) techniques for the deposition of MoS_2 thin films. The PLD approach consists of shining a focused high-power laser beam onto the surface of a solid target to be ablated and deposited as a film on a substrate. PLD is a non-equilibrium process that leads to the absorption of very-short (15–20 ns) and highly-energetic laser pulses by the target and to the formation of a directive plasma plume. The laser-ablated species that form the plasma plume condense onto the substrate, leading to the growth of a thin film. The PLD is well known for its large process latitude, high-flexibility, and excellent process controllability. For instance, by controlling the number of laser ablation pulses and/or the background gas pressure, nanoparticles, and/or films with thicknesses varying from few nm to few microns can be synthesized. Figure 3 shows a schematic representation of a PLD system.
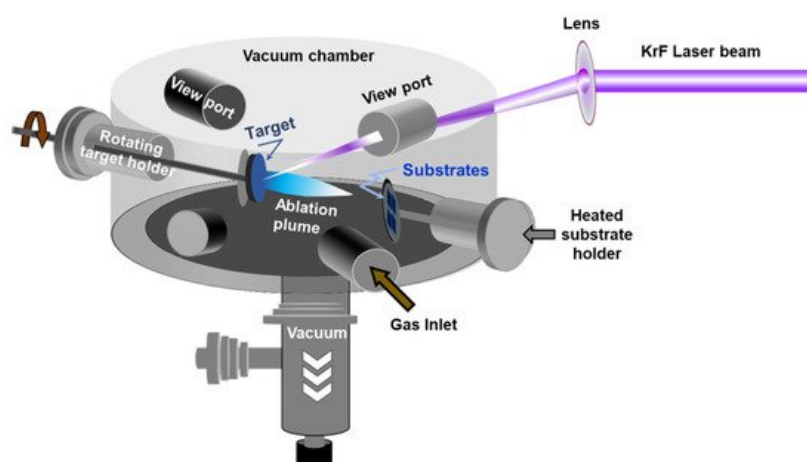

Figure 3. Schematic of the pulsed laser deposition chamber.

Among the advantages and the unique features of the PLD method, we can cite: (i) its ability to achieve a congruent transfer to the films when a multi-element target is used [61]; (ii) its highest instantaneous deposition rate along with the highly-energetic aspect of the ablated species (~10 times higher than in sputtering) enables the growth of metastable phases and/or crystalline phases even at room temperature; and (iii) its process latitude, which makes it easy to control

almost independently each of the deposition parameters (laser intensity, number of laser ablation pulses, background gas pressure, and substrate temperature), and hence the properties of the deposited materials [62][63][64]. While the early studies on the PLD of MoS_2 date back to the 1990s [65][66][67][68][69][70], it is only recently that important advancements have been made in PLD synthesis of 2D-MoS_2 films onto various substrates opening thereby the way to their use for different optoelectronic applications. In 2014, PLD was successfully used to grow one to several layers of MoS_2 onto different metal, semiconducting, and sapphire substrates [71][72]. Siegel et al. [73] were the first to report, in 2015, the growth of MoS_2 films (from 1 to a few 10s of monolayers thick) on centimeter-sized areas. Other attempts were made to deposit ultrathin (≤3 nm) films of nearly-stoichiometric amorphous MoS_2 onto irregular surfaces such as silicon and tungsten tips and to study their field electron emission (FEE) properties [65]. The authors stated that the addition of the MoS_2 coating is beneficial to the FEE process since lower electric fields were required to extract an electron current density of 10 µA/cm^2 (namely, 2.8 V/µm for MoS_2-coated Si and ~5.5 V/µm for MoS_2-coated W tips). More recently, PLD has been used to fabricate high-quality MoS_2 films (monolayer to few layers) and integrated them into functional ultraviolet (UV) photodetectors [74]. The developed photodetectors were found to exhibit a very low dark current (~10 × 10^{-10} A), low operating voltage (2 V), and good response time (32 ms). Their performance surpassed that previously reported for 2D-MoS_2 synthesized by other routes [75][76][77][78][79]. Indeed, under UV irradiation, their detectivity, photoresponse (I_{on}/I_{off} ratio), and responsivity were found to be as high as 1.81 × 10^{14} Jones, 1.37 × 10^5, and 3 × 10^4 A/W, respectively. Table 5 summarizes most of the papers reported so far on the PLD of MoS_2 films. More specifically, it compares the main PLD growth conditions of 2D-MoS_2 films along with the obtained crystallographic phase and some of the reported optoelectronic properties.

Table 5. Summary of the PLD conditions of MoS_2 films along with their thickness and some of their properties.

Substrate	Target	P(Pa)	T(°C)	Laser Energy	Thickness	Properties	Ref
Stainless steel	MoS_2	2.66 × 10^{-6}	RT/200/300/450	5 mJ	≈400 nm	Granular structure stoichiometric, crystalline MoS_2	[80]
Stainless steel	MoS_2	10^{-6}	RT/300	100 mJ	≈70 nm	Stoichiometric single crystal MoS_2	[81]
c-Al_2O_3 (0001) and Si/SiO_2	2H-MoS_2	9.33 × 10^{-4}	600	500 mJ/cm^2	≈1.4 nm	Stoichiometric 2H phase Flake size ≈ 10 µm	[82]
GaN/c-Al_2O_3 (0001)	2H-MoS_2	8 × 10^{-4}	700	50 mJ	Few layers	Mixed phase Roughness ≈0.11 nm	[72]
Titanium foil	p-MoS_2	1.33 × 10^{-2}	RT	–	0.65 nm	1T phase MoS_2	[83]
SiO_2 on Si [70]	MoS_2	1.33 × 10^{-2}	800	200 mJ/cm^2	≈20–60 nm	2H phase MoS_2	[74]
Gold-coated carbon cloth	Amorphous MoS_2	1.33 × 10^{-2}	RT	220 mJ/cm^2	≈200 nm	2H phase MoS_2	[67]
Quartz	MoS_2	9 × 10^{-5}	300	8500 mJ/cm^2	30 layers	Mixed phase	[84]
Al_2O_3 (0001)	MoS_2+S Powder	1.33 × 10^{-2}	700	50 mJ	1–15 Layers of MoS_2	p-MoS_2 2H phase MoS_2 Roughness of 0.27 nm	[71]
Si	MoS_2	4 × 10^{-4}	RT	5/10/100/400 mJ/cm^2	≈100–200 nm	Various compositions of MoS_x (x ≤ 2.2)	[85]
SiO_2	MoS_2	3 × 10^{-5}	700	200 mJ	1–5 layers	2H phase MoS_2	[86]
W (100)-tip	MoS_2+poly(vinl)	5 × 10^{-3}	700	2000 mJ/cm^2	≈20–60 nm	nearly stoichiometric 2H phase MoS_2	[65]
n-Si and p-Si	MoS_2+poly(vinl)	5 × 10^{-3}	700	500 mJ/cm^2	≈20–60 nm	nearly stoichiometric 2H phase MoS_2	[65]

Substrate	Target	P(Pa)	T(°C)	Laser Energy	Thickness	Properties	Ref
Al, Ag, Ni, Cu	MoS_2	2.6×10^{-5}	500	50 mJ	≈5 nm	Epitaxial growth of 2H phase MoS_2	[68]
Sapphire Quartz SiO_2 HfO_2	MoS_2 +S powder	1.33×10^{-2}	700	30 mJ	1 monolayer —2.8 nm	large-area growth of stoichiometric layered 2H phase MoS_2	[87]
SiO_2/Si	MoS_2	10^{-5}	700	200 mJ	few-layer	2H phase MoS_2	[88]
SiO_2/Si	MoS_2 powder	5×10^{-4}	600	2200 mJ/cm^2	13 nm	Epitaxial growth of 2H phase MoS_2	[89]
Si	MoS_2	10^{-4}	RT	100 mJ	129–1900 nm	Stoichiometric films	[90]
c-plane sapphire	MoS_2	10^{-3}	800	2000–3000 mJ/cm^2	1–5 layers	Epitaxial growth of 2H phase MoS_2	[91]
Quartz glass	Polycrystalline MoS_2 powder	5×10^{-4}	300	8500 mJ/cm^2	9–10 monolayers	nearly stoichiometric 2H phase MoS_2	[92]
Quartz	MoS_2	8.9×10^{-5}		600 mJ	≈5.8 nm	2H phase MoS_2	[93]
SiO_2/Si	MoS_2@Ag	1.33×10^{-7}	500	1000–2000 mJ/cm^2	≈1.3–12.8 nm	2H phase MoS_2	[94]
fluorophlogopite mica	MoS_2	10^{-5}	700	4000 mJ/cm^2	≈3.3 nm	2H phase MoS_2	[95]
Al_2O_3 (0001)	MoS_2	10^{-3}	650	100 mJ	≈400 nm	2H phase MoS_2	[96]

2.5. Other Processing Routes

In addition to the main fabrication methods presented above, other PVD techniques have been used to deposit 2D-MoS_2 films. Among these methods, magnetron sputtering has been used to deposit both MoS_2 and WS_2 films onto polydimethylsiloxane (PDMS) polymer substrates [7][97][98][99][100] with controllable defect densities. The PDMS substrate was chosen to fabricate flexible devices based on 2D-semiconducting materials. Interestingly, very smooth MoS_2 surfaces, with a roughness of less than 2 nm, were achieved by casting the polymer on a polished silicon wafer. It has also been shown that it is possible to induce subsequent crystallization of MoS_2 by exposing it to a pulsed 532 nm laser [97].

Finally, the use of any of the above-discussed techniques to fabricate 2D-MoS_2 films is mostly dictated by the availability of the equipment, expertise, and requirements of targeted application. In a general context, the physical-chemical and optoelectronic properties of the final MoS_2 films will be determined to select the appropriate synthesis route. Nevertheless, the level of complexity, throughput, and fabrication costs have to be considered to choose the appropriate synthesis technique particularly when a technology has to be adopted. Table 6 provides a general comparison of the preparation techniques of MoS_2 described in this review by listing their main advantages and limitations.

Table 6. Comparison of the advantages and limitations of different preparation techniques of MoS_2.

Techniques	Advantages	Limitations
Mechanical exfoliation	- High-quality and good crystallinity. - Mono- to few-layer MoS_2 - Simple process	- Long processing time (8–84 h) - Tedious and no controllability - Difficult integration with micro/optoelectronic processing

Techniques	Advantages	Limitations
Chemical exfoliation	- Large-scale growth - Synthesis of MoS_2 monolayer	- Loss of semiconducting properties of MoS_2 during Li intercalation.
Chemical vapor deposition	- High-quality and crystallinity - Centimeter-scale area growth - Good control of morphologies	- Caution due to the use of toxic precursors - High synthesis temperatures requirement - No lateral uniformity - Mixed phases of 1T, 2H, etc.
Atomic layer deposition	- Low-temperature deposition - Uniformity of MoS_2 films - High quality of uniformity - Excellent step coverage	- Very low throughput - Long processing time - High cost
Pulsed laser deposition	- High-quality and faithful transfer of film stoichiometry - Nanometer-level control of the film thickness - Uniformity onto a large surface (up to 3" or 4" diameter wafers) - Quasi-independent control of the growth parameters. - Room-temperature deposition of crystallized MoS_2 - Compatibility with electronic and optoelectronic device processing	- Relatively costly - Presence of ablated particulates on the surface
Sputtering	- High quality and uniformity onto large surface - Compatibility with electronic and optoelectronic device processing. - Fair thickness control	- Relatively costly - Preferential sputtering - Less control on the stoichiometry

3. Characterizations of MoS_2 Thin Films

To assess the crystalline quality, microstructure, and optoelectronic properties of the synthesized 2D-MoS_2, a variety of characterization techniques have been employed and reported in the literature. These include optical microscopy (OM), scanning electron microscopy (SEM), high-resolution transmission and Scanning transmission electron microscopy (HRTEM and HRSTEM), atomic force microscopy (AFM), energy-dispersive X-ray spectroscopy, X-ray photoelectron spectroscopy (XPS), Raman spectroscopy, and photoluminescence (PL). These methods are often used to investigate the overall 2D-MoS_2 surface topography and to qualify the nature of the synthesized material and the shapes of its building blocks (i.e., triangle, nanosheets, and nanoplates) (Figure 4). The observations made by imaging methods are also

essential to envision a possible growth mechanism of the micro/nanostructures with respect to the used processing parameters. For instance, Figure 4d shows a schematic representation of the nucleation process of some morphologies of 2D-MoS$_2$.
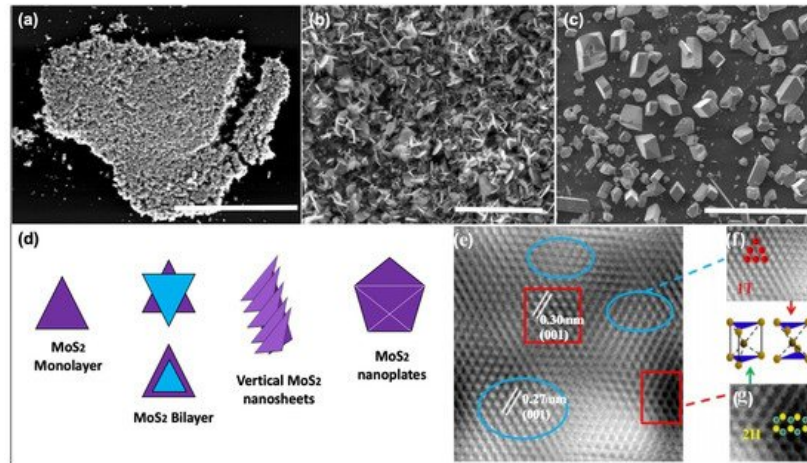

Figure 4. Examples of MoS$_2$ microstructures: (**a**) planar triangle flakes scale = 40 μm; (**b**) vertical nanosheets scale = 100 um; (**c**) vertical nanoplates scale = 100 μm; (**d**) schematic of the nucleation process of MoS$_2$; (**e**) HRTEM image of mixed 1T-MoS$_2$ and 2H-MoS$_2$; (**f**) zoom in of blue circled region of the 1T-MoS$_2$ structure, with the unit cell of the 1T phase; and (**g**) zoom in of red circled region of the 2H-MoS$_2$ structure, with the unit cell of the 2H phase. (Figure 4e–g adapted from Ref. [101] Copyright 2019, Springer Nature.)

Subsequently, HRTEM investigations could be carried out to precisely characterize the MoS$_2$ crystalline structure and examine locally its lattice parameters and the presence of defects. In particular, the HRTEM image depicted in Figure 4e is of great importance, as it was recorded in cross-region containing the two possible crystal configurations of MoS$_2$. As it can be seen in Figure 4e–g, the identified phase mixture of 1T@2H-MoS$_2$ could coexist simultaneously in the same fabricated MoS$_2$ thin film [101].

AFM and its variant methods constitute key characterization tools for the investigation of 2D crystals, mainly due to the atomically thin nature of this layered class of materials. Both vertical and lateral resolutions are fundamentally required to properly investigate the intrinsic properties of 2D materials. AFM is among the few techniques that allow the characterization of 2D-MoS$_2$ in ambient and controlled environments at the nanometer scale. In addition to measuring the local thickness and surface topography, AFM-based electrical methods provide access to additional interesting properties such as the local variations in surface potential of 2D-MoS$_2$. For instance, the Kelvin probe force microscopy (KPFM) method allows the characterization of the sample's surface work function variations. The work function is an extreme surface property, which depends on the energy differences between the Fermi and vacuum levels at the surface. This renders the use of KPFM for the characterization of 2D-MoS$_2$ fundamentally important to investigate band alignments in nanostructures and to study the dependencies of local electronic properties on the number of 2D-MoS$_2$ layers. It also provides key insights into the environmental effects on the state of the sample surface both electronically and morphologically. The KPFM technique was used (Figure 5a) to determine the surface potential variations in mono- and multilayer MoS$_2$, under different humidity conditions.
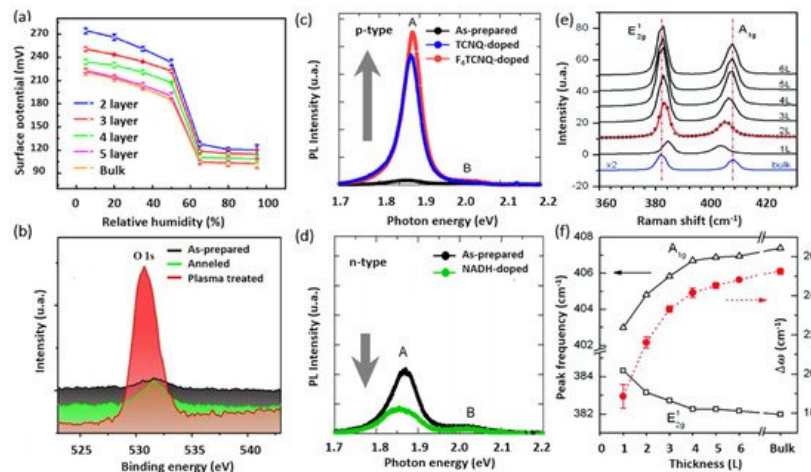
Figure 5. (**a**) Surface potential captured by KPFM vs. relative humidity RHs with respect of the number of MoS_2 layers (reproduced and adapted from Ref. [102], Copyright 2017, IOP Publishing); (**b**) XPS spectra of Mo 3d and S 2s core levels for different treatment conditions (adapted from Ref. [103] Copyright 2014, American Chemical Society); (**c,d**) PL spectra of monolayer MoS_2 before and after being doped (reproduced from Ref. [104] Copyright 2013, American Chemical Society); and (**e,f**) Raman spectra for various MoS_2 films with respect to the number of MoS_2 layers (reproduced from Ref. [105] Copyright 2010, American Chemical Society).

X-ray photoelectron spectroscopy (XPS) is another relevant surface characterization technique that is widely used to achieve the elemental surface composition of MoS_2 films as well as their chemical bonding states. Figure 5b shows typical high-resolution XPS spectra of the Mo_{3d} and S_{2p} core levels. The Mo_{3d} region exhibits two characteristic emission peaks at 232.5 (Mo $3d_{3/2}$) and 229.4 (Mo $3d_{5/2}$) eV. These binding energy values are consistent with electrons of Mo^{4++} corresponding to MoS_2. Likewise, the S $2p_{3/2}$ and S $2p_{1/2}$ doublet appearing at binding energies of 162.3 and 163.5 eV is typical for S^{2-} in MoS_2 structure. Nan et al. [103] used XPS to show the PL enhancement of monolayer MoS_2 through defect engineering and oxygen bonding. The chemical adsorption of oxygen created a heavy p-type doping and the conversion of the Trion into Excitons. Moreover, it caused the suppression of the non-radiative recombination of the excitons at the defect sites. Their results were verified by PL measurements at low temperature, as shown in Figure 5c,d.

Unlike bulk MoS_2, the ultrathin 2D-MoS_2 (i.e., one to few layers) exhibits a strong PL intensity which increases with reducing the number of layers [106], which has been attributed to quantum confinement effects [23][107]. The PL response can be tuned via several mechanisms including doping [104], plasmonic effect, and defects engineering [103]. For instance, Mouri et al. [104] studied the influence of the thickness on the PL response of MoS_2 by using mono-, bi-, and trilayer MoS_2 and the PL modulation using doping. They demonstrated that p-type doping with high electron affinity seems to enhance the PL intensity, while the n-type doping tends to reduce it, as illustrated in Figure 5c,d.

Moreover, Raman spectroscopy presents a very sensitive, fast, and non-destructive technique to access valuable information on the chemical structure, phase and polymorphs, crystallinity, and chemical bonding states of 2D-MoS_2 materials. It allows the monitoring of the two characteristic peaks of MoS_2, namely the in-plane and out-of-plane vibration modes E^1_{2g} and A^1_g appearing for 514 nm excitation energy at the respective positions of 384.5 and 404.6 cm^{-1} for 2D-MoS_2 monolayer [105] (Figure 5e). More interestingly, the difference between the peak positions of E^1_{2g}, A^1_g ($\Delta\omega$) can be used as a robust and effective diagnostic to determine the number of MoS_2 layers (up to four layers) or to simply estimate the MoS_2 film thickness (Figure 5f). Usually, $\Delta\omega$ is less than 20 cm^{-1} in the presence of a single layer of MoS_2, but it increases with increasing MoS_2 thickness to reach 25 cm^{-1} for the bulk MoS_2 [105]. In fact, a thorough study on the dependence of the characteristic Raman peak positions, width, and intensity of MoS_2 films on their thickness have been investigated [73][105][108]. Furthermore, H. Li et al. [108] reported that the frequency of the characteristic peaks is strongly dependent on the excitation energy due to the resonance effect. They showed a red shift of the E^1_{2g} mode of about 2.2 cm^{-1} and blue shift of the A^1_g mode of about 4.1 cm^{-1}. Thus, to effectively determine the exact MoS_2 number of layers using Raman spectroscopy, one has to consider the excitation energy and the thickness limit at which the Raman vibrations frequency is reaching a plateau, indicating that it is less sensitive to MoS_2 thickness variation above four layers.

4. Band Structures and Electronic Properties

We employed density functional theory (DFT) to determine the optoelectronic properties in particular the bandgap energy of both bulk and monolayer MoS_2. Perdew–Burke–Ernzerhof (PBE) approach was applied to describe the electronic states of MoS_2 using band structure and the density of states (DOS). DFT calculations were implemented in Quantum Espresso™ code [109][110]. The considered 2H-MoS_2 has a hexagonal crystal form with the space group P63/mmc (No. 194). The equivalent positions for this structure employed in the calculations are Mo (1/3, 2/3, and 2/8) and S (1/3, 2/3, and 0.621). The valence electron configuration selected for Mo and S atoms are $4p^5 5s^1$ and $3s^2 3p^4$, respectively. The cutoff wave function and the cutoff charge densities are 70 and 700 Ryd, respectively [110]. The cell parameters and atomic positions were fully relaxed by the process of the total energy minimization. The values of the relaxed lattice constants for bulk MoS_2 are a = 3.15 Å and c = 12.3 Å, respectively. The optimized structure was used to perform calculations for band structures and the total density of states for both MoS_2 bulk and monolayer. For bulk MoS_2 (top left panel of Figure 6a), 9 × 9 ×2 k-points were used to obtain the band structure along the path Γ-K-M-Γ in the Brillouin zone. For MoS_2 monolayer (top right panel of Figure 6a), 9 × 9 × 1 k-points were used. A 15 Å vacuum along the z-axis above the monolayer was added to isolate the MoS_2 and prevent any interaction between the adjacent layers [111]. The top view of the MoS_2 monolayer is shown in the bottom panel of Figure 6a, where sulfur atoms are represented in yellow and molybdenum atoms are shown in purple.
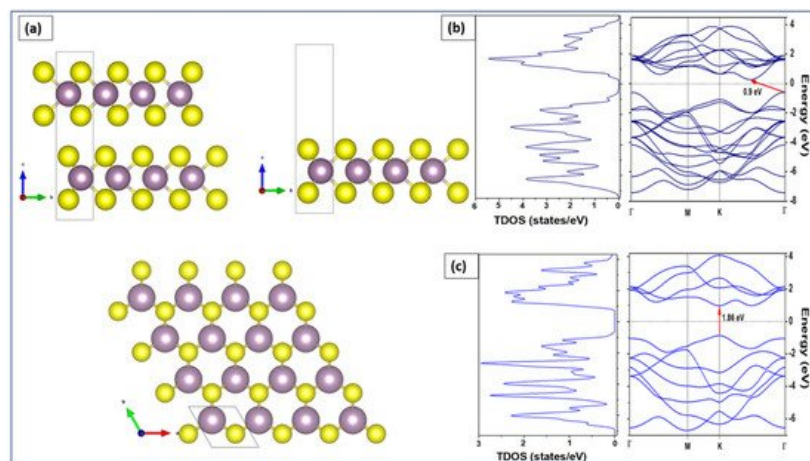
Figure 6. (**a**) Bulk MoS$_2$ (**top-left**), monolayer MoS$_2$ (**top-right**), and top view of MoS$_2$ monolayer (**bottom**). Total density of states (**left**) and band structure (**right**) of the (**b**) bulk and (**c**) monolayer.

To obtain the electronic properties, the MoS$_2$ bulk was considered as a set of two hexagonal planes linked together by weak Van Der Waals bonds. The MoS$_2$ monolayer was considered as a single hexagonal plane with covalent bonds between atoms S-Mo-S [112]. The left panel of Figure 6b shows the total DOS calculation results of the bulk MoS$_2$ while the right panel of Figure 6b shows the calculation of its band structure. The energy range is between −8 and 4 eV versus the directions of the highest symmetries in the first Brillouin zone Γ, M, K, and Γ. As observed from the band structure calculations, the MoS$_2$ bulk has an indirect bandgap of 0.9 eV. The minimum of the conduction band is located between K and G and the maximum of valence band at point G. This indirect bandgap obtained for the MoS$_2$ bulk was attributed to the presence of interlayer interactions in the bulk structure [113]. In contrast, Figure 6c shows that the monolayer MoS$_2$ has a direct bandgap of 1.89 eV at the K point. The DOS results are compatible with the results of the band structure. Similar conclusions have been stated in other investigations [111][112].

References

1. Xu, H.; Yi, J.; She, X.; Liu, Q.; Song, L.; Chen, S.; Yang, Y.; Song, Y.; Vajtai, R.; Lou, J.; et al. 2D heterostructure comprised of metallic 1T-MoS2/Monolayer O-g-C3N4 towards efficient photocatalytic hydrogen evolution. Appl. Catal. B Environ. 2018, 220, 379–385.

2. Backes, C.; Berner, N.C.; Chen, X.; Lafargue, P.; LaPlace, P.; Freeley, M.; Duesberg, G.S.; Coleman, J.N.; McDonald, A.R. Functionalization of liquid-exfoliated two-dimensional 2H-MoS2. Angew. Chemie - Int. Ed. 2015, 54, 2638–2642.

3. Tan, D.; Willatzen, M.; Wang, Z.L. Prediction of strong piezoelectricity in 3R-MoS2 multilayer structures. Nano Energy 2019, 56, 512–515.

4. Liu, K.K.; Zhang, W.; Lee, Y.H.; Lin, Y.C.; Chang, M.T.; Su, C.Y.; Chang, C.S.; Li, H.; Shi, Y.; Zhang, H.; et al. Growth of large-area and highly crystalline MoS 2 thin layers on insulating substrates. Nano Lett. 2012, 12, 1538–1544.

5. Yu, H.; Liao, M.; Zhao, W.; Liu, G.; Zhou, X.J.; Wei, Z.; Xu, X.; Liu, K.; Hu, Z.; Deng, K.; et al. Wafer-Scale Growth and Transfer of Highly-Oriented Monolayer MoS2 Continuous Films. ACS Nano 2017, 11, 12001–12007.

6. Yang, P.; Zhang, S.; Pan, S.; Tang, B.; Liang, Y.; Zhao, X.; Zhang, Z.; Shi, J.; Huan, Y.; Shi, Y.; et al. Epitaxial Growth of Centimeter-Scale Single-Crystal MoS2 Monolayer on Au(111). ACS Nano 2020, 14, 5036–5045.

7. Chen, X.P.; Xing, G.J.; Xu, L.F.; Lian, H.Q.; Wang, Y. Vertically aligned MoS2 films prepared by RF-magnetron sputtering method as electrocatalysts for hydrogen evolution reactions. Compos. Interfaces 2020, 1–10.

8. Hu, Z.; Wang, L.; Zhang, K.; Wang, J.; Cheng, F.; Tao, Z.; Chen, J. MoS2 Nanoflowers with Expanded Interlayers as High-Performance Anodes for Sodium-Ion Batteries. Angew. Chemie - Int. Ed. 2014, 53, 12794–12798.

9. Chen, J.; Kuriyama, N.; Yuan, H.; Takeshita, H.T.; Sakai, T. Electrochemical hydrogen storage in MoS2 nanotubes. J. Am. Chem. Soc. 2001, 123, 11813–11814.

10. Li, W.J.; Shi, E.W.; Ko, J.M.; Chen, Z.Z.; Ogino, H.; Fukuda, T. Hydrothermal synthesis of MoS2 nanowires. J. Cryst. Growth 2003, 250, 418–422.

11. Hwang, H.; Kim, H.; Cho, J. MoS2 nanoplates consisting of disordered graphene-like layers for high rate lithium battery anode materials. Nano Lett. 2011, 11, 4826–4830.

12. Deokar, G.; Vancsó, P.; Arenal, R.; Ravaux, F.; Casanova-Cháfer, J.; Llobet, E.; Makarova, A.; Vyalikh, D.; Struzzi, C.; Lambin, P.; et al. MoS2–Carbon Nanotube Hybrid Material Growth and Gas Sensing. Adv. Mater. Interfaces 2017, 4, 1–10.

13. Deokar, G.; Vignaud, D.; Arenal, R.; Louette, P.; Colomer, J. Synthesis and characterization of MoS2 nanosheets. Nanotechnology 2016, 27, 075604.

14. Deokar, G.; Rajput, N.S.; Vancsó, P.; Ravaux, F.; Jouiad, M.; Vignaud, D.; Cecchet, F.; Colomer, J.F. Large area growth of vertically aligned luminescent MoS2 nanosheets. Nanoscale 2017, 9, 277–287.

15. Gan, X.; Gao, Y.; Fai Mak, K.; Yao, X.; Shiue, R.J.; Van Der Zande, A.; Trusheim, M.E.; Hatami, F.; Heinz, T.F.; Hone, J.; et al. Controlling the spontaneous emission rate of monolayer MoS2 in a photonic crystal nanocavity. Appl. Phys. Lett. 2013, 103, 181119.

16. Eda, G.; Fujita, T.; Yamaguchi, H.; Voiry, D.; Chen, M.; Chhowalla, M. Coherent atomic and electronic heterostructures of single-layer MoS 2. ACS Nano 2012, 6, 7311–7317.

17. Wang, T.; Chen, S.; Pang, H.; Xue, H.; Yu, Y. MoS2-Based Nanocomposites for Electrochemical Energy Storage. Adv. Sci. 2017, 4, 1600289.

18. Shokri, A.; Salami, N. Gas sensor based on MoS2 monolayer. Sensors Actuators, B Chem. 2016, 236, 378–385.

19. Deokar, G.; Rajput, N.S.; Li, J.; Deepak, F.L.; Ou-Yang, W.; Reckinger, N.; Bittencourt, C.; Colomer, J.F.; Jouiad, M. Toward the use of CVD-grown MoS2 nanosheets as field-emission source. Beilstein J. Nanotechnol. 2018, 9, 1686–1694.

20. Ma, J.; Bai, H.; Zhao, W.; Yuan, Y.; Zhang, K. High efficiency graphene/MoS2/Si Schottky barrier solar cells using layer-controlled MoS2 films. Sol. Energy 2018, 160, 76–84.

21. Arulraj, A.; Ramesh, M.; Subramanian, B.; Senguttuvan, G. In-situ temperature and thickness control grown 2D-MoS2 via pulsed laser ablation for photovoltaic devices. Sol. Energy 2018, 174, 286–295.

22. Guo, F.; Li, M.; Ren, H.; Huang, X.; Hou, W.; Wang, C.; Shi, W.; Lu, C. Fabrication of p-n CuBi2O4/MoS2 heterojunction with nanosheets-on-microrods structure for enhanced photocatalytic activity towards tetracycline degradation. Appl. Surf. Sci. 2019, 491, 88–94.

23. Splendiani, A.; Sun, L.; Zhang, Y.; Li, T.; Kim, J.; Chim, C.Y.; Galli, G.; Wang, F. Emerging photoluminescence in monolayer MoS2. Nano Lett. 2010, 10, 1271–1275.

24. Eda, G.; Yamaguchi, H.; Voiry, D.; Fujita, T.; Chen, M.; Chhowalla, M. Photoluminescence from chemically exfoliated MoS 2. Nano Lett. 2011, 11, 5111–5116.

25. Rafiee, J.; Mi, X.; Gullapalli, H.; Thomas, A.V.; Yavari, F.; Shi, Y.; Ajayan, P.M.; Koratkar, N.A. Wetting transparency of graphene. Nat. Mater. 2012, 11, 217–222.

26. Kozbial, A.; Zhou, F.; Li, Z.; Liu, H.; Li, L. Are Graphitic Surfaces Hydrophobic? Acc. Chem. Res. 2016, 49, 2765–2773.

27. Marbou, K.; Ghaferi, A.A.; Jouiad, M. In-situ Characterization of Wettability Alteration in HOPG. SOP Trans. Nanotechnol 2015, 2374, 1–10.

28. Huang, Y.; Pan, Y.H.; Yang, R.; Bao, L.H.; Meng, L.; Luo, H.L.; Cai, Y.Q.; Liu, G.D.; Zhao, W.J.; Zhou, Z.; et al. Universal mechanical exfoliation of large-area 2D crystals. Nat. Commun. 2020, 11, 1–9.

29. Magda, G.Z.; Petõ, J.; Dobrik, G.; Hwang, C.; Biró, L.P.; Tapasztó, L. Exfoliation of large-area transition metal chalcogenide single layers. Sci. Rep. 2015, 5, 3–7.

30. Kim, S.; Park, W.; Kim, D.; Kang, J.; Lee, J.; Jang, H.Y.; Song, S.H.; Cho, B.; Lee, D. Novel exfoliation of high-quality 2h-mos2 nanoflakes for solution-processed photodetector. Nanomaterials 2020, 10, 1045.

31. Pirzado, A.A.; Le Normand, F.; Romero, T.; Paszkiewicz, S.; Papaefthimiou, V.; Ihiawakrim, D.; Janowska, I. Few-layer graphene from mechanical exfoliation of graphite-based materials: Structure-dependent characteristics. ChemEngineering 2019, 3, 1–10.

32. Novoselov, K.S.; Jiang, D.; Schedin, F.; Booth, T.J.; Khotkevich, V.V.; Morozov, S.V.; Geim, A.K.; Benka, S.G. Two-dimensional atomic crystals. Phys. Today 2005, 58, 9.

33. Janica, I.; Iglesias, D.; Ippolito, S.; Ciesielski, A.; Samorì, P. Effect of temperature and exfoliation time on the properties of chemically exfoliated MoS2nanosheets. Chem. Commun. 2020, 56, 15573–15576.

34. Guan, Z.; Wang, C.; Li, W.; Luo, S.; Yao, Y.; Yu, S.; Sun, R.; Wong, C.P. A facile and clean process for exfoliating MoS2 nanosheets assisted by a surface active agent in aqueous solution. Nanotechnology 2018, 29, 425702.

35. Lin, H.; Wang, J.; Luo, Q.; Peng, H.; Luo, C.; Qi, R.; Huang, R.; Travas-Sejdic, J.; Duan, C.G. Rapid and highly efficient chemical exfoliation of layered MoS2and WS2. J. Alloys Compd. 2017, 699, 222–229.

36. Yang, Y.Q.; Tye, C.T.; Smith, K.J. Influence of MoS2 catalyst morphology on the hydrodeoxygenation of phenols. Catal. Commun. 2008, 9, 1364–1368.

37. Liu, H.F.; Wong, S.L.; Chi, D.Z. CVD Growth of MoS2-based Two-dimensional Materials. Chem. Vap. Depos. 2015, 21, 241–259.

38. Wang, Q.H.; Kalantar-Zadeh, K.; Kis, A.; Coleman, J.N.; Strano, M.S. Electronics and optoelectronics of two-dimensional transition metal dichalcogenides. Nat. Nanotechnol. 2012, 7, 699–712.

39. Zeng, T.; You, Y.; Wang, X.; Hu, T.; Tai, G. Chemical vapor deposition and device application of two-dimensional molybdenum disulfide-based atomic crystals. Prog. Chem. 2016, 28, 459–470.

40. Balendhran, S.; Ou, J.Z.; Bhaskaran, M.; Sriram, S.; Ippolito, S.; Vasic, Z.; Kats, E.; Bhargava, S.; Zhuiykov, S.; Kalantar-Zadeh, K. Atomically thin layers of MoS 2via a two step thermal evaporation-exfoliation method. Nanoscale 2012, 4, 461–466.

41. Nam Trung, T.; Kamand, F.Z.; Al tahtamouni, T.M. Elucidating the mechanism for the chemical vapor deposition growth of vertical MoO2/MoS2 flakes toward photoelectrochemical applications. Appl. Surf. Sci. 2020, 505, 144551.

42. Ahn, C.; Lee, J.; Kim, H.U.; Bark, H.; Jeon, M.; Ryu, G.H.; Lee, Z.; Yeom, G.Y.; Kim, K.; Jung, J.; et al. Low-Temperature Synthesis of Large-Scale Molybdenum Disulfide Thin Films Directly on a Plastic Substrate Using Plasma-Enhanced Chemical Vapor Deposition. Adv. Mater. 2015, 27, 5223–5229.

43. Sojková, M.; Siffalovic, P.; Babchenko, O.; Vanko, G.; Dobročka, E.; Hagara, J.; Mrkyvkova, N.; Majková, E.; Ižák, T.; Kromka, A.; et al. Carbide-free one-zone sulfurization method grows thin MoS 2 layers on polycrystalline CVD diamond. Sci. Rep. 2019, 9, 2–12.

44. Withanage, S.S.; Kalita, H.; Chung, H.S.; Roy, T.; Jung, Y.; Khondaker, S.I. Uniform Vapor-Pressure-Based Chemical Vapor Deposition Growth of MoS2 Using MoO3 Thin Film as a Precursor for Coevaporation. ACS Omega 2018, 3, 18943–18949.

45. Wang, S.; Rong, Y.; Fan, Y.; Pacios, M.; Bhaskaran, H.; He, K.; Warner, J.H. Shape evolution of monolayer MoS2 crystals grown by chemical vapor deposition. Chem. Mater. 2014, 26, 6371–6379.

46. Jeon, J.; Jang, S.K.; Jeon, S.M.; Yoo, G.; Jang, Y.H.; Park, J.H.; Lee, S. Layer-controlled CVD growth of large-area two-dimensional MoS2 films. Nanoscale 2015, 7, 1688–1695.

47. Hyun, C.M.; Choi, J.H.; Lee, S.W.; Park, J.H.; Lee, K.T.; Ahn, J.H. Synthesis mechanism of MoS2 layered crystals by chemical vapor deposition using MoO3 and sulfur powders. J. Alloys Compd. 2018, 765, 380–384.

48. Lin, Z.; Zhao, Y.; Zhou, C.; Zhong, R.; Wang, X.; Tsang, Y.H.; Chai, Y. Controllable Growth of Large-Size Crystalline MoS2 and Resist-Free Transfer Assisted with a Cu Thin Film. Sci. Rep. 2015, 5, 1–10.

49. Rotunno, E.; Bosi, M.; Seravalli, L.; Salviati, G.; Fabbri, F. Influence of organic promoter gradient on the MoS2growth dynamics. Nanoscale Adv. 2020, 2, 2352–2362.

50. Le, D.; Rawal, T.B.; Rahman, T.S. Single-Layer MoS2 with Sulfur Vacancies: Structure and Catalytic Application. J. Phys. Chem. C 2014, 118, 5346–5351.

51. Jurca, T.; Moody, M.J.; Henning, A.; Emery, J.D.; Wang, B.; Tan, J.M.; Lohr, T.L.; Lauhon, L.J.; Marks, T.J. Low-Temperature Atomic Layer Deposition of MoS2 Films. Angew. Chemie - Int. Ed. 2017, 56, 4991–4995.

52. Tan, L.K.; Liu, B.; Teng, J.H.; Guo, S.; Low, H.Y.; Loh, K.P. Atomic layer deposition of a MoS2 film. Nanoscale 2014, 6, 10584–10588.

53. Mattinen, M.; Hatanpää, T.; Sarnet, T.; Mizohata, K.; Meinander, K.; King, P.J.; Khriachtchev, L.; Räisänen, J.; Ritala, M.; Leskelä, M. Atomic Layer Deposition of Crystalline MoS2 Thin Films: New Molybdenum Precursor for Low-Temperature Film Growth. Adv. Mater. Interfaces 2017, 4, 1700123.

54. Jin, Z.; Shin, S.; Kwon, D.H.; Han, S.J.; Min, Y.S. Novel chemical route for atomic layer deposition of MoS2 thin film on SiO2/Si substrate. Nanoscale 2014, 6, 14453–14458.

55. Browning, R.; Padigi, P.; Solanki, R.; Tweet, D.J.; Schuele, P.; Evans, D. Atomic layer deposition of MoS2 thin films. Mater. Res. Express 2015, 2, 12–17.

56. Liu, H.; Chen, L.; Zhu, H.; Sun, Q.Q.; Ding, S.J.; Zhou, P.; Zhang, D.W. Atomic layer deposited 2D MoS2 atomic crystals: From material to circuit. Nano Res. 2020, 13, 1644–1650.

57. Chen, C.; Raza, M.H.; Amsalem, P.; Schultz, T.; Koch, N.; Pinna, N. Morphology-Controlled MoS2 by Low-Temperature Atomic Layer Deposition. Nanoscale 2020, 12, 20404–20412.

58. Yang, J.; Liu, L. Nanotribological properties of 2-D MoS2 on different substrates made by atomic layer deposition (ALD). Appl. Surf. Sci. 2020, 502, 144402.

59. Huang, Y.; Liu, L.; Sha, J.; Chen, Y. Size-dependent piezoelectricity of molybdenum disulfide (MoS2) films obtained by atomic layer deposition (ALD). Appl. Phys. Lett. 2017, 111, 063902.

60. Jang, Y.; Yeo, S.; Lee, H.B.R.; Kim, H.; Kim, S.H. Wafer-scale, conformal and direct growth of MoS 2 thin films by atomic layer deposition. Appl. Surf. Sci. 2016, 365, 160–165.

61. Pandiyan, R.; Oulad Elhmaidi, Z.; Sekkat, Z.; Abd-lefdil, M.; El Khakani, M.A. Reconstructing the energy band electronic structure of pulsed laser deposited CZTS thin films intended for solar cell absorber applications. Appl. Surf. Sci. 2017, 396, 1562–1570.

62. Brassard, D.; El Khakani, M.A. Pulsed-laser deposition of high- k titanium silicate thin films. J. Appl. Phys. 2005, 98, 054912.

63. Daghrir, R.; Drogui, P.; Dimboukou-Mpira, A.; El Khakani, M.A. Photoelectrocatalytic degradation of carbamazepine using Ti/TiO2 nanostructured electrodes deposited by means of a pulsed laser deposition process. Chemosphere 2013, 93, 2756–2766.

64. Ka, I.; Le Borgne, V.; Ma, D.; El Khakani, M.A. Pulsed laser ablation based direct synthesis of single-wall carbon nanotube/PbS quantum dot nanohybrids exhibiting strong, spectrally wide and fast photoresponse. Adv. Mater. 2012, 24, 6289–6294.

65. Late, D.J.; Shaikh, P.A.; Khare, R.; Kashid, R.V.; Chaudhary, M.; More, M.A.; Ogale, S.B. Pulsed laser-deposited MoS2 thin films on W and Si: Field emission and photoresponse studies. ACS Appl. Mater. Interfaces 2014, 6, 15881–15888.

66. Rai, R.H.; Pérez-Pacheco, A.; Quispe-Siccha, R.; Glavin, N.R.; Muratore, C. Pulsed laser annealing of amorphous two-dimensional transition metal dichalcogenides. J. Vac. Sci. Technol. A 2020, 38, 052201.

67. Wang, R.; Sun, P.; Wang, H.; Wang, X. Pulsed laser deposition of amorphous molybdenum disulfide films for efficient hydrogen evolution reaction. Electrochim. Acta 2017, 258, 876–882.

68. Loh, T.A.J.; Chua, D.H.C. Growth mechanism of pulsed laser fabricated few-layer MoS2 on metal substrates. ACS Appl. Mater. Interfaces 2014, 6, 15966–15971.

69. McDevitt, N.T.; Bultman, J.E.; Zabinski, J.S. Study of amorphous MoS2 films grown by pulsed laser deposition. Appl. Spectrosc. 1998, 52, 1160–1164.

70. Mosleh, M.; Laube, S.J.P.; Suh, N.P. Friction of undulated surfaces coated with mos2 by pulsed laser deposition. Tribol. Trans. 1999, 42, 495–502.

71. Serrao, C.R.; Diamond, A.M.; Hsu, S.L.; You, L.; Gadgil, S.; Clarkson, J.; Carraro, C.; Maboudian, R.; Hu, C.; Salahuddin, S. Highly crystalline MoS2 thin films grown by pulsed laser deposition. Appl. Phys. Lett. 2015, 106, 052101.

72. Barvat, A.; Prakash, N.; Singh, D.K.; Dogra, A.; Khanna, S.P.; Singh, S.; Pal, P. Mixed Phase Compositions of MoS2 Ultra Thin Film Grown by Pulsed Laser Deposition. Mater. Today Proc. 2018, 5, 2241–2245.

73. Siegel, G.; Venkata Subbaiah, Y.P.; Prestgard, M.C.; Tiwari, A. Growth of centimeter-scale atomically thin MoSfilms by pulsed laser deposition. APL Mater. 2015, 3, 056103.

74. Kumar, S.; Sharma, A.; Ho, Y.T.; Pandey, A.; Tomar, M.; Kapoor, A.K.; Chang, E.Y.; Gupta, V. High performance UV photodetector based on MoS2 layers grown by pulsed laser deposition technique. J. Alloys Compd. 2020, 835, 155222.

75. Lopez-Sanchez, O.; Lembke, D.; Kayci, M.; Radenovic, A.; Kis, A. Ultrasensitive photodetectors based on monolayer MoS 2. Nat. Nanotechnol. 2013, 8, 497–501.

76. Alkis, S.; Öztaş, T.; Aygün, L.E.; Bozkurt, F.; Okyay, A.K.; Ortaç, B. Thin film MoS_2 nanocrystal based ultraviolet photodetector. Opt. Express 2012, 20, 21815.

77. Huo, N.; Konstantatos, G. Ultrasensitive all-2D MoS2 phototransistors enabled by an out-of-plane MoS2 PN homojunction. Nat. Commun. 2017, 8, 1–6.

78. Tsai, D.S.; Liu, K.K.; Lien, D.H.; Tsai, M.L.; Kang, C.F.; Lin, C.A.; Li, L.J.; He, J.H. Few-layer MoS2 with high broadband photogain and fast optical switching for use in harsh environments. ACS Nano 2013, 7, 3905–3911.

79. Goel, N.; Kumar, R.; Roul, B.; Kumar, M.; Krupanidhi, S.B. Wafer-scale synthesis of a uniform film of few-layer MoS2 on GaN for 2D heterojunction ultraviolet photodetector. J. Phys. D. Appl. Phys. 2018, 51, 374003.

80. Donley, M.S.; Murray, P.T.; Barber, S.A.; Haas, T.W. Deposition and properties of MoS2 thin films grown by pulsed laser evaporation. Surf. Coatings Technol. 1988, 36, 329–340.

81. Walck, S.D.; Donley, M.S.; Zabinski, J.S.; Dyhouse, V.J. Characterization of Pulsed Laser Deposited PbO/MoS2 by Transmission Electron Microscopy. J. Mater. Res. 1994, 9, 236–245.

82. Barvat, A.; Prakash, N.; Satpati, B.; Singha, S.S.; Kumar, G.; Singh, D.K.; Dogra, A.; Khanna, S.P.; Singha, A.; Pal, P. Emerging photoluminescence from bilayer large-area 2D MoS2 films grown by pulsed laser deposition on different substrates. J. Appl. Phys. 2017, 122, 015304.

83. Wang, R.; Shao, Q.; Yuan, Q.; Sun, P.; Nie, R.; Wang, X. Direct growth of high-content 1T phase MoS2 film by pulsed laser deposition for hydrogen evolution reaction. Appl. Surf. Sci. 2020, 504, 144320.

84. Wang, S.; Yu, H.; Zhang, H.; Wang, A.; Zhao, M.; Chen, Y.; Mei, L.; Wang, J. Broadband few-layer MoS2 saturable absorbers. Adv. Mater. 2014, 26, 3538–3544.

85. Fominski, V.Y.; Markeev, A.M.; Nevolin, V.N.; Prokopenko, V.B.; Vrublevski, A.R. Pulsed laser deposition of MoSx films in a buffer gas atmosphere. Thin Solid Films 1994, 248, 240–246.

86. Jiao, L.; Jie, W.; Yang, Z.; Wang, Y.; Chen, Z.; Zhang, X.; Tang, W.; Wu, Z.; Hao, J. Layer-dependent photoresponse of 2D MoS 2 films prepared by pulsed laser deposition. J. Mater. Chem. C 2019, 7, 2522–2529.

87. Serna, M.I.; Yoo, S.H.; Moreno, S.; Xi, Y.; Oviedo, J.P.; Choi, H.; Alshareef, H.N.; Kim, M.J.; Minary-Jolandan, M.; Quevedo-Lopez, M.A. Large-Area Deposition of MoS2 by Pulsed Laser Deposition with in Situ Thickness Control. ACS Nano 2016, 10, 6054–6061.

88. Jiao, L.; Wang, Y.; Zhi, Y.; Cui, W.; Chen, Z.; Zhang, X.; Jie, W.; Wu, Z. Fabrication and Characterization of Two-Dimensional Layered MoS2 Thin Films by Pulsed Laser Deposition. Adv. Condens. Matter Phys. 2018, 2018, 23–28.

89. Pradhan, G.; Sharma, A.K. Anomalous Raman and photoluminescence blue shift in mono- and a few layered pulsed laser deposited MoS2 thin films. Mater. Res. Bull. 2018, 102, 406–411.

90. Walck, S.D.; Zabinski, J.S.; Donley, M.S.; Bultman, J.E. Evolution of surface topography in pulsed-laser-deposited thin films of MoS2. Surf. Coatings Technol. 1993, 62, 412–416.

91. Ho, Y.T.; Ma, C.H.; Luong, T.T.; Wei, L.L.; Yen, T.C.; Hsu, W.T.; Chang, W.H.; Chu, Y.C.; Tu, Y.Y.; Pande, K.P.; et al. Layered MoS2 grown on c -sapphire by pulsed laser deposition. Phys. Status Solidi - Rapid Res. Lett. 2015, 9, 187–191.

92. Zhang, Y.; Wang, S.; Yu, H.; Zhang, H.; Chen, Y.; Mei, L.; Di Lieto, A.; Tonelli, M.; Wang, J. Atomic-layer molybdenum sulfide optical modulator for visible coherent light. Sci. Rep. 2015, 5, 1–7.

93. Zhang, Y.; Wang, S.; Wang, D.; Yu, H.; Zhang, H.; Chen, Y.; Mei, L.; Di Lieto, A.; Tonelli, M.; Wang, J. Atomic-layer molybdenum sulfide passively modulated green laser pulses. IEEE Photonics Technol. Lett. 2016, 28, 197–200.

94. Miao, P.; Ma, Y.; Sun, M.; Li, J.; Xu, P. Tuning the SERS activity and plasmon-driven reduction of p-nitrothiophenol on a film. Faraday Discuss. 2019, 214, 297–307.

95. Xie, M.Z.; Zhou, J.Y.; Ji, H.; Ye, Y.; Wang, X.; Jiang, K.; Shang, L.Y.; Hu, Z.G.; Chu, J.H. Annealing effects on sulfur vacancies and electronic transport of MoS2 films grown by pulsed-laser deposition. Appl. Phys. Lett. 2019, 115, 121901.

96. Su, B.; He, H.; Ye, Z. Large-area ZnO/MoS2 heterostructure grown by pulsed laser deposition. Mater. Lett. 2019, 253, 187–190.

97. Pang, X.; Zhang, Q.; Shao, Y.; Liu, M.; Zhang, D.; Zhao, Y. A flexible pressure sensor based on magnetron sputtered mos2. Sensors (Switzerland) 2021, 21, 1130.

98. Tao, J.; Chai, J.; Lu, X.; Wong, L.M.; Wong, T.I.; Pan, J.; Xiong, Q.; Chi, D.; Wang, S. Growth of wafer-scale MoS2 monolayer by magnetron sputtering. Nanoscale 2015, 7, 2497–2503.

99. Kaindl, R.; Bayer, B.C.; Resel, R.; Müller, T.; Skalakova, V.; Habler, G.; Abart, R.; Cherevan, A.S.; Eder, D.; Blatter, M.; et al. Growth, structure and stability of sputter-deposited MoS2 thin films. Beilstein J. Nanotechnol. 2017, 8, 1115–1126.

100. Rowley-Neale, S.J.; Ratova, M.; Fugita, L.T.N.; Smith, G.C.; Gaffar, A.; Kulczyk-Malecka, J.; Kelly, P.J.; Banks, C.E. Magnetron Sputter-Coated Nanoparticle MoS2 Supported on Nanocarbon: A Highly Efficient Electrocatalyst toward the Hydrogen Evolution Reaction. ACS Omega 2018, 3, 7235–7242.

101. Tian, L.; Wu, R.; Liu, H.Y. Synthesis of Au-nanoparticle-loaded 2 nanosheets with high photocatalytic performance. J. Mater. Sci. 2019, 54, 9656–9665.

102. Feng, Y.; Zhang, K.; Li, H.; Wang, F.; Zhou, B.; Fang, M.; Wang, W.; Wei, J.; Wong, H.S.P. In situ visualization and detection of surface potential variation of mono and multilayer MoS2 under different humidities using Kelvin probe force microscopy. Nanotechnology 2017, 28, 295705.

103. Nan, H.; Wang, Z.; Wang, W.; Liang, Z.; Lu, Y.; Chen, Q.; He, D.; Tan, P.; Miao, F.; Wang, X.; et al. Strong photoluminescence enhancement of MoS2 through defect engineering and oxygen bonding. ACS Nano 2014, 8, 5738–5745.

104. Mouri, S.; Miyauchi, Y.; Matsuda, K. Tunable Photoluminescence of Monolayer MoS2 via Chemical Doping. Nano Lett. 2013, 13, 5944–5948.

105. Lee, C.; Yan, H.; Brus, L.E.; Heinz, T.F.; Hone, J.; Ryu, S. Anomalous lattice vibrations of single- and few-layer MoS2. ACS Nano 2010, 4, 2695–2700.

106. Mak, K.F.; Lee, C.; Hone, J.; Shan, J.; Heinz, T.F. Atomically thin MoS2: A new direct-gap semiconductor. Phys. Rev. Lett. 2010, 105, 2–5.

107. Cheiwchanchamnangij, T.; Lambrecht, W.R.L. Quasiparticle band structure calculation of monolayer, bilayer, and bulk MoS 2. Phys. Rev. B - Condens. Matter Mater. Phys. 2012, 85, 205302.

108. Li, H.; Zhang, Q.; Yap, C.C.R.; Tay, B.K.; Edwin, T.H.T.; Olivier, A.; Baillargeat, D. From bulk to monolayer MoS 2: Evolution of Raman scattering. Adv. Funct. Mater. 2012, 22, 1385–1390.

109. Ahmad, S.; Mukherjee, S. A Comparative Study of Electronic Properties of Bulk MoS2 and Its Monolayer Using DFT Technique: Application of Mechanical Strain on MoS2 Monolayer. Graphene 2014, 03, 52–59.

110. Erfanifam, S.; Jamilpanah, L.; Sangpour, P.; Haddadi, F.; Hamdi, M.; Erfanifam, M.; Chanda, G.; Herrmannsdörfer, T.; Sazgari, V.; Sadeghi, A.; et al. Electrical and optical properties of MoS2,MoOx=2,3(MoSO)/RGO heterostructure. arXiv 2018, 3, 1–6.

111. Zhang, Z.; Qian, Q.; Li, B.; Chen, K.J. Interface Engineering of Monolayer MoS2/GaN Hybrid Heterostructure: Modified Band Alignment for Photocatalytic Water Splitting Application by Nitridation Treatment. ACS Appl. Mater. Interfaces 2018, 10, 17419–17426.

112. Dolui, K.; Rungger, I.; Das Pemmaraju, C.; Sanvito, S. Possible doping strategies for MoS2 monolayers: An ab initio study. Phys. Rev. B - Condens. Matter Mater. Phys. 2013, 88, 075420.

113. Zahid, F.; Liu, L.; Zhu, Y.; Wang, J.; Guo, H. A generic tight-binding model for monolayer, bilayer and bulk MoS 2. AIP Adv. 2013, 3, 052111.